Electronic Supplementary Material (ESI) for Physical Chemistry Chemical Physics.

Supplementary Materials for

The Reaction of Criegee Intermediate CH_2OO with Water Dimer: Primary Products and Atmospheric Impact

Leonid Sheps, Brandon Rotavera, Arkke J. Eskola, David L. Osborn, Craig A. Taatjes, Kendrew Au, Dudley E. Shallcross, M. Anwar H. Khan, and Carl J. Percival

Correspondence to: lsheps@sandia.gov

This PDF file includes:

SupplementaryText
Figures S1 to S7
Table S1

A. EXPERIMENTAL ANALYSIS

A1. Time evolution of product ions at m/z = 46 in PIMS measurements

The ion peak at m/z = 46 contains contributions from CH_2OO and formic acid, HCOOH. The time evolution of this peak as a function of water concentration is shown in Fig. S2, along with kinetic fit results (thick lines). The fitting procedure, based on equation E6 of the main text, was identical to that employed for the UV absorption results.

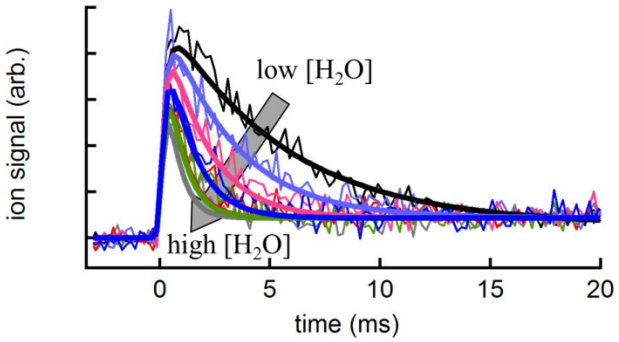

Figure S1. Representative PIMS ion signals at m/z = 46 at varying [H_2O], taken at the ionization energy of hν = 11.5 eV. Thin lines are the experimental data; thick lines are kinetic fits using equation E1.

A2. Time evolution and relative yield measurements of products at m/z = 47

The time evolution of the m/z = 47 ion peak typically has a rapid signal rise followed by a decay to a stable signal plateau. Three representative time traces of this ion peak, from no added [H_2O] to fairly high [H_2O], are shown in Fig. S2. These traces reveal two separate contributions to the m/z = 47 signal. The first is from a product that is formed even under dry conditions and does not decay quickly; the second is from a transient species that depends on the presence of water and decays within ~20 ms.

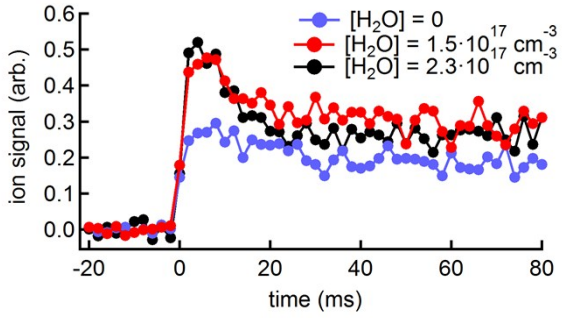

Figure S2. Typical time evolution of the m/z = 47 ion signal at hν = 11.5 eV. The experimental conditions are: P = 30 Torr (He), [O_2] = $2.6 \cdot 10^{16}$ cm^{-3}, [CH_2I_2] = $7.6 \cdot 10^{12}$ cm^{-3}, $[CH_2OO]_{t=0} \sim 9 \cdot 10^{11}$ cm^{-3}, [H_2O] = 0 – $2.3 \cdot 10^{17}$ cm^{-3}.

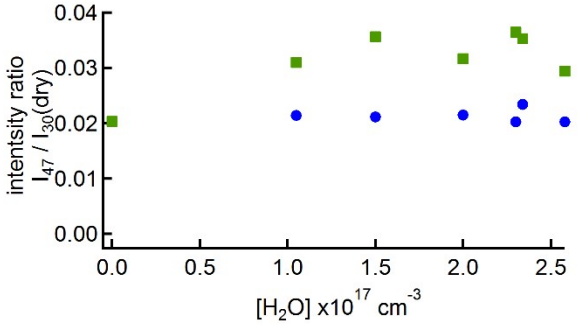

Figure S3. Maximum (early-time, green) and long-time (t = 70 – 80 ms, blue) intensity of the m/z = 47 peak at hν = 11.5 eV, normalized to that of CH_2O under dry conditions.

The maximum intensity of the m/z = 47 ion peak is plotted vs. water concentration in Fig. S3, along with the intensity of the signal plateau at t = 70 – 80 ms. All signals are normalized to that of the formaldehyde peak (m/z = 30) at dry conditions. The maximum intensity at $[H_2O] = 0$ comes only from the stable (non-decaying) signal component, whereas the maximum intensity at $[H_2O] > 0$ is the sum of both components. The stable ion signal is nearly constant in all experiments; the rapidly decaying signal is absent at $[H_2O] = 0$ but is relatively independent of water concentration at $[H_2O] > 0$. When $[H_2O]$ increases from $1 \cdot 10^{17}$ cm^{-3} to $2.6 \cdot 10^{17}$ cm^{-3}, the value of F^{dimer} grows from ~0.45 to ~0.81, whereas F^{mono} remains at ~0.06. We therefore conclude that the slowly decaying ion signal does not come from reactions that involve water, whereas the fast component likely arises from the reaction of CH_2OO with the water monomer. The intensity of either component is 1 – 2 % compared to that of CH_2O.

A3. Rise time of main product ion peaks

Figure S4 shows the time evolution of PIMS signals of products in the reaction R3, arbitrarily scaled for visual comparison. Panel A shows CH_2O and HMHP traces taken at $[H_2O] = 1.1 \cdot 10^{17}$ cm^{-3} and $2.6 \cdot 10^{17}$ cm^{-3}, along with a CH_2O trace at $[H_2O] = 0$ cm^{-3}. Panel A also shows simulated exponential rise traces (solid, dotted, and dashed black lines), with rate coefficients k_{rise} listed next to the line. At $[H_2O] = 0$, CH_2O rises with k_{rise} ~180 s^{-1}, which matches the 180 s^{-1} decay rate coefficient of CH_2OO (see Table 2, main test, experimental set #3). The rate coefficient for CH_2OO decay at the other two H_2O concentrations in panel A is 375 s^{-1} and 1300 s^{-1}; Fig S4 includes simulated time traces to illustrate what product signals with k_{rise} = 375 s^{-1} and 1300 s^{-1} would look like. However, we find instead that at all $[H_2O] > 0$ all product signals have k_{rise} ~220 s^{-1}, as shown in panel B. The rise times of CH_2O and HMHP signals (circles and triangles, respectively) match at all values of $[H_2O]$. Clearly, the measured product k_{rise} of 220 s^{-1} is independent of $[H_2O]$ and is substantially slower than CH_2OO decay at all $[H_2O] > 0$.This suggests that $CH_2OO + (H_2O)_2$ forms a complex which dissociates with a rate coefficient ~220 s^{-1} at room T; the measured product rise times likely correspond to the decay of the complex rather than the decay of CH_2OO. However, we did not directly detect such a complex, which would have a parent cation at m/z = 82 in PIMS experiments.

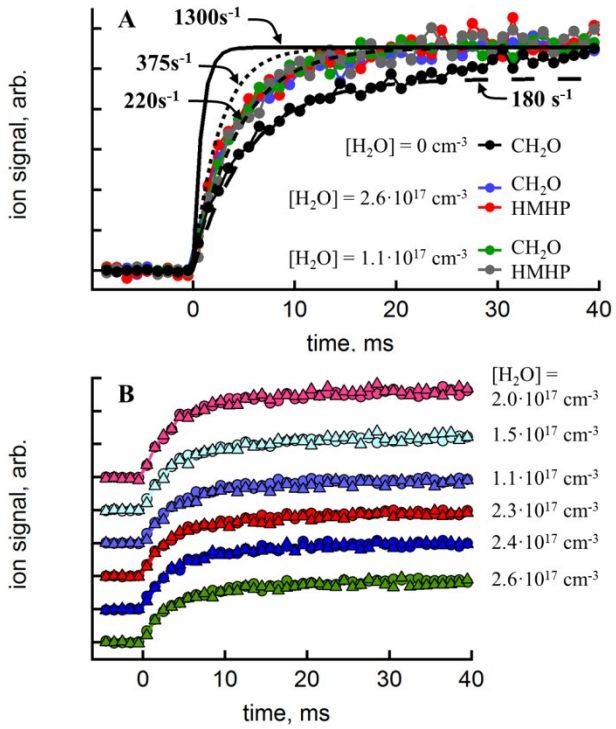

Figure S4. Time evolution of the main product ion signals in R3 at varying [H_2O]. CH_2O signals are from the *m*/*z*=30 ion peak; HMHP signals are sums of *m*/*z*=31 and 64 peaks. The ion signals are scaled arbitrarily to compare their rise times. *Panel A:* time evolution of CH_2O at [H_2O] = 0 (black circles); CH_2O and HMHP at [H_2O] = $2.6 \cdot 10^{17}$ cm^{-3} (blue and red circles, respectively); CH_2O and HMHP at [H_2O] = $1.1 \cdot 10^{17}$ cm^{-3} (green and gray circles, respectively). Solid, dotted, and dashed black lines are exponential rise functions with the pseudo first-order rate coefficient listed next to each line. *Panel B:* time evolution of CH_2O (circles) and HMHP (triangles) at varying [H_2O].

A4. Potential effect of wall reactions on observed reaction kinetics

A4.1 General solution for diffusion and wall losses in cylindrical symmetry

Time profiles of transient chemical species in the PIMS apparatus can in principle be affected by gas-phase diffusion and by wall reactions (if wall reactions convert reactants into products more rapidly than diffusion can replenish them). The observed depletion of the reactants at the sidewall can be modeled analytically by analogy to the heat transfer formulae[1] for cylindrical symmetry, assuming that the initial reactant distribution within the reactor is uniform. The general solution is:

$$\Theta(r,t) = \sum_{i=1}^{\infty} e^{-\frac{D_X}{a^2}\beta_i^2 t} \frac{2BJ_0(\frac{r}{a}\beta_i)}{\{\beta_i^2 + B^2\}J_0(\beta_i)} \qquad \text{(ES1)}$$

where $\Theta(r,t)$ is the dimensionless concentration of species X at radial distance *r* and time *t*, $\Theta = \frac{[X] - [X]_\infty}{[X]_0 - [X]_\infty}$;

$[X]_0$ and $[X]_\infty$ are the initial and final concentrations, respectively;

a is the radius of the reactor;

D_X is the gas-phase diffusion coefficient of species X;

$\{\beta_i\}$ are the roots of the characteristic equation for this problem:

$$\beta J_1(\beta) - B J_0(\beta) = 0 \tag{ES2}$$

J_0 and J_1 are Bessel functions of the first kind (of order 0 and 1, respectively);

B is the Biot number.

The Biot number, B, is the ratio of transport efficiency across the reactor boundary to that within the reactor medium.[1] For mass transfer problems, B is expressed as

$$B = \frac{-\dot{n}_X a}{A_{wall}[X] D_X} \tag{ES3}$$

$$\dot{n}_X = \frac{dn_X}{dt} = \frac{d[X]}{dt} V \tag{ES4}$$

where $-\dot{n}_X$ is the total mass flux of X in the reactor of volume V across a boundary with surface area A_{wall}. For a cylindrical reactor the ratio of volume to surface area is

$$\frac{V}{A_{wall}} = \frac{\pi a^2 z}{2\pi a z} = \frac{a}{2} \tag{ES5}$$

If species X undergoes wall reactions or losses with a first-order rate coefficient k_{wall}, its concentration decays as follows:

$$\frac{d[X]}{dt} = -k_{wall}[X] \tag{ES6}$$

equations ES3 – ES6 can then be rearranged to write the Biot number in terms of k_{wall} and a gas-phase diffusion coefficient D_X:

$$B = \frac{k_{wall} a^2}{2 D_X} \tag{ES7}$$

Although the sum in equation ES1 is over $i = 1 - \infty$, in practice the first few terms of this sum usually provide a close approximation to the exact solution. Bessel functions, as well as the eigenvalues set $\{\beta\}$ have been extensively tabulated; hence, the apparent reactant depletion at the reactor wall, $\Theta(r{=}a,t)$ can be readily visualized if the diffusion and wall reaction rate coefficients are known. Unfortunately, for the reactions in our study neither D nor k_{wall} are known for any of the possible reactants (CH_2OO or the CH_2OO complex with water monomer or dimer) or products (HCOOH, CH_2O, HMHP). Nevertheless, we can estimate the necessary diffusion coefficients using the method of Fuller *et al.*[2] and examine certain limiting cases of k_{wall} to assess the possible influence of the wall reactions on our results.

A4.2 Effects of CH_2OO diffusion and wall reactions

In the approach of Fuller *et al.*,[2] the binary diffusion coefficient D_{AB} for species A and B can be estimated using the reduced mass M_{AB} and diffusion volumes Σ_A and Σ_B:

$$D_{AB} = \frac{0.00143 T^{1.75}}{P M_{AB}^{1/2} \left[\Sigma_A^{1/3} + \Sigma_B^{1/3}\right]^2} \tag{ES8}$$

where P is the pressure in bar and $M_{AB} = 2\left[M_A^{-1} + M_B^{-1}\right]^{-1}$. Diffusion volumes Σ_{He} and Σ_{H2O} have been determined reliably as 2.67 and 13.1, respectively; the diffusion volume of CH_2OO may be estimated by summing over atomic contributions as $\Sigma_{CH2OO} = 32.7$.[3] Using equation ES8, $D(CH_2OO)$ at total P = 30 Torr is ~14 cm^2s^{-1} for pure He bath and ~5 cm^2s^{-1} for pure H_2O vapor. CH_2OO is a trace species diffusing into a homogeneous environment; therefore, $D(CH_2OO)$ can be calculated for He/H_2O mixtures with molar fractions χ_{He} and χ_{H2O}, assuming Blanc's law:[3] $D_{mix} = \left[\chi_{He}/D_{He} + \chi_{H2O}/D_{H2O}\right]^{-1}$. We note that diffusion in H_2O vapor is likely severely overestimated, since ES8 neglects the effects of polarity or hydrogen bonding. Nonetheless, $D(CH_2OO)$ can be estimated in this work to range from ~ 14 cm^2s^{-1} at dry conditions to <8 cm^2s^{-1} at maximum [H_2O].
The key question here is whether the observed CH_2OO decays at a range of [H_2O] are the result of gas-phase or surface reactions. The effective CH_2OO decay rate coefficient k_4 in PIMS experiments with halocarbon wax reactor coating (datasets #2 and #3) was ~180 s^{-1} at [H_2O] = 0. Based on literature reports,[4,5] CH_2OO self-reaction accounts for apparent first-order loss of ~110 s^{-1}; thus the wall loss rate coefficient in datasets #2 and #3 was even smaller, ~70 s^{-1}. Figure S5 shows modeled CH_2OO loss at the reactor wall for two values of $D(CH_2OO)$, 8 and 14 cm^2s^{-1}, and three values of k_{wall}, 70, 300, and 1000 s^{-1}. According to the model, wall loss rate coefficient k_{wall} = 70 s^{-1} results in observed decays that deviate only slightly from single exponential decays with the same k; such deviation should be imperceptible within the signal-to-noise ratio of our data. However, faster wall losses produce obviously non-exponential traces with increasingly rapid decay within the first 1 – 2 ms after photolysis. Signal decays at later times, on the other hand, are largely controlled by the gas-phase diffusion, with apparent rate coefficients of ~150 s^{-1}, even for much larger values of k_{wall}.

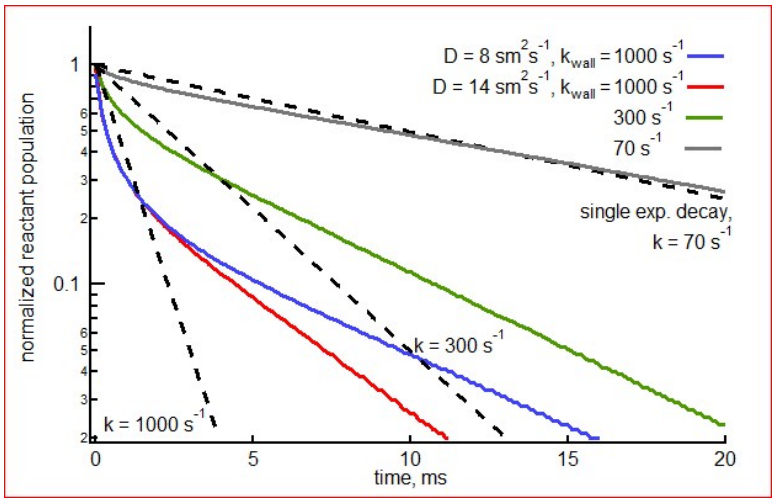

Figure S5. Simulated normalized reactant concentrations at the reactor wall. The solid lines show the model results using equation ES1 with diffusion coefficient D = 8 cm^2s^{-1} or 14 cm^2s^{-1} and wall loss rate coefficient k_{wall} = 70, 300, or 1000 s^{-1}. The dashed lines show single exponential decays with rate coefficients k = 70, 300, or 1000 s^{-1}.

Fig. S1 and Fig. 2 of the main text show that CH_2OO ion signal in our PIMS experiments exhibit nearly single exponential decays with timescales that agree very well with those obtained by the TR-BB-CEAS probing in a larger reactor and with those reported in the

literature. Fig. S5, meanwhile, shows that such agreement would not be possible if the reaction $CH_2OO + (H_2O)_2$ occurred on the reactor wall. Together, these observations indicate that, at a minimum, the $CH_2OO–(H_2O)_2$ complex formation occurs in the gas phase, with negligible interference from heterogeneous processes.

A4.3 Effects of diffusion and wall reactions on the $CH_2OO–(H_2O)_2$ complex

The products of the title reaction form with rate coefficients of ~220 s^{-1}, irrespective of $[H_2O]$, which implies a metastable intermediate complex, $CH_2OO–(H_2O)_2$. We must therefore also consider possible wall effects on the decomposition of this complex, i.e. whether this occurs in the gas phase or on the reactor wall. The $CH_2OO–(H_2O)_2$ diffusion volume can be estimated by the method of Fuller *at al.*[2] as $\Sigma_{complex} = 54.2$. The resulting diffusion coefficient is $D(CH_2OO–(H_2O)_2)$ ~11 cm^2s^{-1} at very low $[H_2O]$ and <6 cm^2s^{-1} at the highest $[H_2O]$ in our study.

Figure S6 shows how diffusion and wall losses affect the $CH_2OO–(H_2O)_2$ population near the reactor wall. Using realistic values of $D(CH_2OO–(H_2O)_2) < 11$ cm^2s^{-1} results in non-exponential time traces that are largely diffusion-limited at $t > 1 – 2$ ms. Such decays of the intermediate complex would in turn lead to non-exponential rising signals for reaction products, in disagreement with Figure S4. Furthermore, products yields obtained in PIMS dataset #1 are consistent with those from datasets #2 and #3, despite the difference in reactor wall coating. These observations suggest that $CH_2OO–(H_2O)_2$ decomposition also occurs in the gas-phase and that wall effects are negligible.

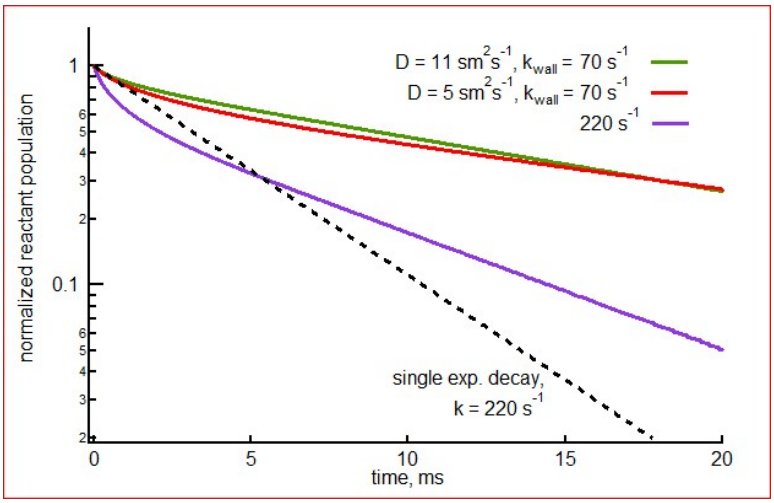

Figure S6. Simulated normalized reactant concentrations at the reactor wall, using $D = 5$ cm^2s^{-1} or 11 cm^2s^{-1} and wall loss rate coefficient $k_{wall} = 70$ or 220 s^{-1}. The dashed line shows a single exponential decay with a rate coefficient $k = 220$ s^{-1}.

References

1 D. W. Hahn and M. N. Özişik, *Heat Conduction Fundamentals*, 3rd edn., John Wiley & Sons, Hoboken, NJ, USA, 2012.

2 E. N. Fuller, P. D. Schettler and J. C. Giddings, *Industrial & Engineering Chemistry*, 1966, **58**, 18-27.

3 B. E. Poling, J. M. Prausnitz and J. P. O'connell, *The properties of gases and liquids*, 5th edn., Mcgraw-hill New York, 2001.
4 W.-L. Ting, C.-H. Chang, Y.-F. Lee, H. Matsui, Y.-P. Lee and J. J.-M. Lin, *J. Chem. Phys.*, 2014, **141**, 104308.
5 Z. J. Buras, R. M. Elsamra and W. H. Green, *J. Phys. Chem. Lett.*, 2014, **5**, 2224-2228.

B. The Global Chemistry Transport Model CRI-STOCHEM

The following papers describe model results and their comparison with a variety of field data: Archibald *et al.*,[1] Cooke *et al.*,[2-3] Henne *et al.*,[4] Bacak *et al.*,[5] Utembe *et al.*[6,7] The description of the model is broken down into two parts; the meteorological module and the chemical module, which are presented in subsections II and III, respectively. The model was originally described in Collins *et al.*,[8] with updates described by Derwent *et al.*,[9] with a new extended chemical scheme and an organic aerosol module described in Watson *et al.*,[10] Jenkin *et al.*,[11] and Utembe *et al.*[12]

B1. General Aspects

STOCHEM is a global 3-dimensional chemistry transport model in which 50,000 constant mass air parcels are advected using a Lagrangian approach allowing the chemistry and transport processes to be uncoupled. STOCHEM is an "offline" model with the transport and radiation codes driven by archived meteorological data, generated by the UKMO Unified Model (UM) at a climate resolution of 1.25^{o} longitude × 0.83^{o} latitude × 12 unevenly spaced vertical levels.[13] Archived meteorological data contains pressure, temperatures, humidities, winds, tropopause heights, cloud, precipitation, boundary layer and surface parameters.[14]

B2. Meteorological Parameterizations

B2.1 Vertical Coordinate

The vertical coordinate used in STOCHEM is a hybrid pressure coordinate, η, originally described in Simmons and Burridge[15] and used in the Meteorological Office Unified model. The hybrid pressure coordinate is calculated using the following equation (SE1)

$$\eta = (P/P_s) + A(1/P_0 - 1/P_s) \qquad \text{(SE1)}$$

where P is the pressure of a given air parcel, P_s is the surface pressure, P_0 is the reference pressure (1000 hPa) and A is a coefficient with the dimensions of pressure.

B2.2 Advection Scheme

The 50,000 constant mass Lagrangian air parcels are advected using wind fields generated by the UK Meteorological office unified model (UM).[16] The archived meteorological data used is for the year 1998 at a resolution of 1.25^{0} longitude × 0.83^{0} latitude × 12 vertical levels between the surface and about 100 mb. The archived meteorology contains 6 hourly wind fields containing horizontal winds (v_x and v_y), and vertical winds (v_η). The advection time step is set to three hours so the meteorological wind fields (6 hourly) are linearly interpolated with respect to time. The 3-dimensional spatial interpolation uses a cubic polynomial in the vertical direction and a bi-linear method is used for the horizontal components.[17] A fourth order Runge-Kutta method is used to solve the ordinary differential equation to calculate the new position of each Lagrangian cell at the end of each time step. The temperature, pressure and humidity of the cells are calculated by 3-dimensional interpolation in an analogous manner to the wind fields after the advection step.

B3. Chemical Module

B3.1 Chemical Mechanism

The chemical mechanism used is the common representative intermediates mechanism version 2 and reduction 5 (CRI v2-R5). Its generation and validation are described in detail in the papers Watson *et al.*,[10] Jenkin *et al.*,[11] and Utembe *et al.*[12] The CRI scheme was devised from a reduction of the Master Chemical Mechanism (MCM) and is a near-explicit chemical mechanism originally described by Jenkin *et al.*[14] The construction is broken down into three parts as shown in Figure S5. The initiation reactions of a VOC are photolysis, reaction with OH, reaction with NO_3 and reaction with ozone. Not all VOCs undergo all reactions, for instance no reaction between ozone and an alkane has been observed. The products of the initiation reactions are predominantly peroxy radicals which are oxidised to give a range of species as shown in Figure S5.

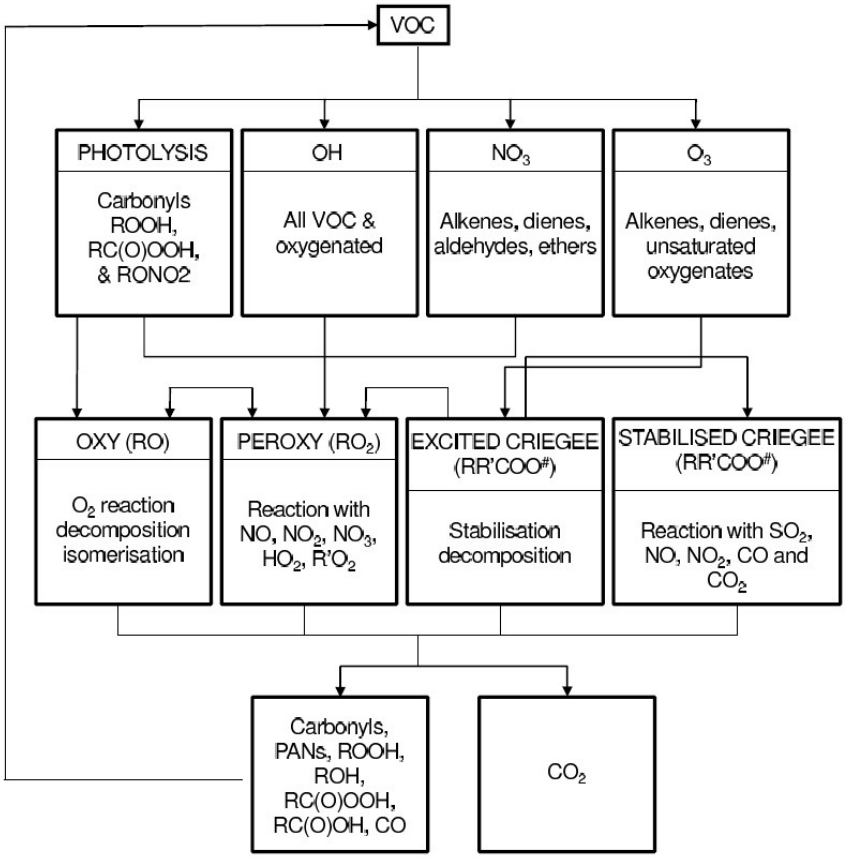

Figure S7: Chemistry used in the construction of the MCM.[18] Oxidation reactions are broken down into initiation, propagation (reactions of intermediates) and termination (formation of products).

The products formed by this scheme are oxidised themselves until they are lost from the system or form CO_2. The MCM v3.1 is the third version of the master chemical mechanism which has undergone improvements because of developments in the understanding of mechanistic processes. The MCM v3.1 describes the degradation of 130 emitted VOCs. Due to its near-explicit nature the MCM v3.1 consists of 5900 species competing in 13500 (photo)chemical reactions. Such a large mechanism is impractical for

use in a global or regional scale model due to computational limitations. Therefore, a series of reduced mechanisms were produced using the MCM v3.1 as a reference benchmark.[10-12] A key assumption of the reduction methodology is that the potential for ozone formation of a given VOC is related to the total number of reactive bonds (i.e. C-H and C-C bonds).[19] This allowed a series of generic intermediates to be defined which are "common representatives" for a large set of species. The resultant reduced mechanism used here (CRI v2-R5) represents the degradation of methane and 22 emitted VOCs using 196 species competing in 555 photochemical reactions and gives excellent agreement with the MCM v3.1 over a full range of NOx levels.[10,11] The secondary organic aerosol (SOA) scheme that was then developed from this mechanism is described in detail in Utembe *et al.*[12]

B3.2 Calculation of CI

During the integration the concentration of stabilized CI (Criegee Intermediates) are calculated using the steady state assumption where the total production rate (the sum of the terms $k_x[\text{alkene}_x][O_3]\Gamma_{SCI(X)}$, where k_x is the rate coefficient for the reaction of alkene_x with ozone and $\Gamma_{SCI(X)}$ is the fraction of stabilized CI formed)is divided by the total loss rate ($k_4 + k_5[NO_2] + k_6[SO_2] + k_2[H_2O] + k_3[(H_2O)_2]$), where k_4 is the unimolecular loss rate for an CI (assigned a value of 200 s^{-1}), and k_2, k_3, k_5, k_6 are rate coefficients for reaction of the CI with H_2O, $(H_2O)_2$, NO_2, and SO_2.

B3.3 Photolysis

The photolysis rate of a given species is calculated using the following integral.

$$J_A = \int_0^\infty F(\lambda)\sigma_A(\lambda)\Phi_A(\lambda)d\lambda \qquad \text{(SE2)}$$

where J_A is the photolysis rate of compound A, $F(\lambda)$ is the spherically integrated actinic flux at a given wavelength, $\sigma_A(\lambda)$ is the absorption cross section of compound A at a given wavelength λ and $\Phi_A(\lambda)$ is the quantum yield for dissociation of A at a given wavelength. The integral is restricted to tropospherically relevant wavelengths and for computational efficiency the integral is replaced by a sum over all wavelengths. The cross section and quantum yields are taken from the recommendations of either the Jet Propulsion Laboratory (JPL) kinetic evaluation reports[20,21] or the International Union of Pure and Applied Chemistry (IUPAC) data evaluations.[22] Spherically integrated actinic fluxes are calculated over 106 wavelength intervals within the range 200 - 660 nm for a given air parcel using a variant of the two stream model developed by Hough.[23] This representation uses measured values for the solar flux with attenuation of the photons being calculated for a range of factors. These attenuation factors include absorption in and above the stratosphere by O_2 and O_3, absorption by O_2 and O_3 in the troposphere, absorption and scattering (reflection and refraction) by aerosol and clouds, scatter by other gas phase molecules in the troposphere and the surface albedo. The method is a two stream representation as upwards and downwards fluxes are calculated to evaluate the incident light at a given point. The photolysis rate for each reaction is calculated explicitly for each air parcel at a time resolution of one hour. The one hourly photolysis

rates are linearly interpolated with respect to time to achieve five minute resolution values which are used in the chemical integration.

B4. Emissions

There are three types of emissions featured in STOCHEM; surface emissions, stratospheric sources and 3-dimensional emissions. Emissions from the surface from biomass burning, vegetation, oceans, soil and 'other' surface emissions are distributed using monthly two dimensional source maps at a resolution of 5° longitude by 5° latitude.[24] The anthropogenic surface distributions for CH_4, CO, NOx and VOCs have been developed for the year 2000 by the International Institute for Applied Systems Analysis (IIASA) and are described in detail by Cofala *et al.*[25] Emissions totals for CO, NO_x and NMVOCs are taken from the Precursor of ozone and their Effects in the Troposphere (POET) inventory[26] for the year 1998. Emission totals for CH_4 have been taken from the inverse model study of Mikaloff-Fletcher *et al.*,[27] except for the ocean emissions which are from Houweling *et al.*[28] The anthropogenic and biomass burning emissions of the aromatic species o-xylene, benzene and toluene were taken from Henze *et al.*[29] Biomass burning emissions of ethyne, formaldehyde and acetic acid are produced using scaling factors from Andreae and Merlet[30] per mole CO emitted. The primary organic aerosol (POA) anthropogenic global total was taken from the AEROCOM dataset using the totals from fossil fuels and biofuel burning.[31]

The POA biomass burning global total was taken from the GFED v2.1 dataset.[32] The annual emission totals for each compound in a given category are shown in Table S1. Isoprene is unique among the biogenic hydrocarbons because of its direct relationship to photosynthetic activity of plants.[33] This is not the case with other biogenically emitted species such as terpenes whose emissions continue at night. Therefore the surface emissions of isoprene within STOCHEM are emitted at a rate proportional to the cosine of the solar zenith angle during the day, with no emissions at night. The rate is adjusted so an appropriate amount is emitted per month and thus per year adding up to the global total of 501 Tg/yr shown in Table S1. The Lagrangian cells within the model are kept below 100 hPa whereas in reality there would be exchange between the troposphere and stratosphere. In order to represent this air exchange a simulated net downward flux of ozone and HNO_3 into the top level of the model is calculated using 3-hourly vertical wind fields and monthly ozone fields from Li and Shine.[34] These emissions are distributed on a resolution of 5° longitude by 5° latitude at a vertical coordinate of $\eta = 0.1$. Based on the work of Murphy and Fahey[35] the HNO_3 flux is calculated as one thousandth of the ozone flux by mass of N. Lightning and aircraft emissions are not surface emissions and are distributed in a 3-dimensional manner within the model. The distributions for lightning emissions are parameterized based on the work of Price and Rind[36] with the emissions being distributed evenly between the convective cloud top height and the surface. The lightning emissions are input on a resolution of 5° longitude by 5° latitude at a vertical resolution of $\eta = 0.1$. The emissions are scaled so that the global total NO_x emission from lightning is 5 Tg(N)/yr. The NO_x emissions from civil and military aircraft are taken from NASA inventories for 1992.[34] The implementation of the emissions from aircraft is the same as for lightning with an annual total of 0.85 Tg(N)/yr. All emissions are converted into units of molecules per second per grid square and are implemented as an additional

term in the production flux for a given chemical species. The emission flux is implemented during the chemistry time step.

Table S1.
Global emission totals in Tg/yr, except NO_x and HNO_3 which are in Tg(N)/yr, and SO_2 which is in Tg(S)/yr. The "Other" emission for CH_4 includes paddys (56 Tg/yr), wetlands (220 Tg/yr), termites (16 Tg/yr) and other animals (87 Tg/yr).

Species	Anthropogenic	Biomass burning	Vegetation	Soil	Oceans	Other
NO_x	30.5	6.8	8.0	5.6		5.9
CO	570.1	472.0	160.0		20.0	
CH_4	133.0	88.0			15.0	379.0
HCHO	1.2	3.6				
H_2	20.0	20.0		5.0	5.0	
C_2H_6	5.7	3.2	0.8		0.8	
CH_3CHO	1.8	3.6				
C_4H_{10}	53.3	1.1	8.0			
SO_2	56.6	2.2				8.8
C_2H_4	4.2	6.3	4.3		1.2	
C_3H_6	2.0	1.9	0.9		1.3	
o-xylene	4.0	0.7				
C_3H_8	6.4	0.6	1.6		1.1	
CH_3OH	1.0	9.2	229.5			
Acetone	0.3	1.8	15.0			
Isoprene			501.0			
Toluene	5.3	1.6				
α-pinene			84.7			
β-pinene			42.3			
Benzene	3.1	2.5				
HCOOH	1.8	5.5				
CH_3COOH	16.8	3.2				
C_2H_5OH	2.8	0.3				
MEK	1.1	4.2				
C_2H_5CHO	1.6					
C_2H_2	4.0	1.7				
t-but-2-ene	5.7	1.6				

B5. Dry and Wet Deposition

When Lagrangian cells are located in the boundary layer the species within these air parcels can be lost by wet and dry deposition. The rate of dry deposition is dependent on whether the air parcel is over land or ocean with appropriate species dependent deposition velocities. This representation can be extended to include differences between types of land surface, such as savannah and forest. Dry deposition velocities for each species are calculated using equations SE3 and SE4

$$F_A = c_A v_d / H \qquad \text{(SE3)}$$

where F_A is the dry deposition flux of species A, c_A is the concentration of species A, v_d is the deposition velocity of species A and H is the height above the ground, and

$$v_d = (v_1 \times v_a) / (v_1 + v_a) \qquad \text{(SE4)}$$

where v_d and v_1 represent the species dependent deposition velocity at 50 m and at 1 m, respectively and v_a is the relative aerodynamic deposition velocity between 1 m and 50 m. In this implementation the assumption is made that species deposition velocities at 50 m are representative of a given species deposition velocity throughout the mixed boundary layer. Soluble species can be removed from the atmosphere by precipitation referred to commonly as wet deposition. Species dependent scavenging coefficients for convective and dynamic precipitation are taken from Penner *et al.*[37] These coefficients are combined with precipitation rates and scavenging profiles to calculate loss rates of each species from an air parcel. Precipitation rates at a given point in the atmosphere are calculated using the dynamic precipitation, convective precipitation and convective cloud top heights read in from the meteorology.

B6. Aerosol module

An organic aerosol module suitable for use with the CRI v2 and all reduced variants has been developed by Utembe *et al.*[11] POA is directly emitted into the atmosphere and is removed by wet and dry deposition. The method, briefly described here, for SOA formation has been used previously with the MCM[38-42] giving good agreement with both field and chamber measurements. For a more detailed description of the methodology see Johnson *et al.*[42] The formation of SOA is represented by a species dependent dynamic equilibrium between the gas and aerosol phases, equation SE5.

$$C_a/C_g = K_p C_{om} \qquad \text{(SE5)}$$

where C_a is the concentration of a given species in the aerosol phase, C_g is the concentration of a given species in the gas phase, K_p is the partitioning coefficient (μg m^{-3}) and C_{om} is the total mass concentration of condensed organic material. K_p is evaluated using the absorptive partitioning theory of Pankow,[43] equation SE6.

$$Kp = \frac{7.501 \times 10^{-9} RT}{MW_{om} \zeta P_L^o} \qquad \text{(SE6)}$$

where R is the gas constant (8.314 J K^{-1} mol^{-1}), T is the temperature (in K), MW_{om} is the mean molecular weight of the absorbing particulate organic material (g mol^{-1}), ζ is the activity coefficient of the species in the condensed phase and P_L^o is its liquid vapour pressure (in Torr). ζ is set to unity for all species as it is expected that aerosol particles comprise mixtures of similar types of molecules. The vapour pressures for many of the species in the MCM have not been measured and therefore an estimation method was employed. An extended semi-empirical form of the Clausius-Clapeyron equation was applied along with estimated values of species boiling temperature (Tb) and entropy change of vaporisation at that temperature ($\Delta S_{vap}(Tb)$). Tb was estimated for a given species using the fragmentation method of Stein and Brown.[44] ΔSvap(Tb) values were estimated using the methodology of Baum.[45] Utembe *et al.*[12] used a photochemical trajectory model to produce a reduced representation of secondary organic aerosol (SOA) formation which is compatible with all six versions of the CRI v2, including reduction 5 used in these studies. The TORCH-2003 campaign in the south-east UK in late July and early August of 2003 resulted in the production of a comprehensive measurement dataset of VOCs, NOx, Ozone and Organic Aerosol.[40,41] A photochemical trajectory model was initially run with the MCM v3.1 coupled with the parameterized gas to aerosol absorptive partitioning method (equation SE5) for about 2000 closed shell species for evaluation against the measurements made during TORCH-2003.[11] The MCM v3.1 organic aerosol representation was thus reduced to 365 low volatility species which represented >95% by mass of the simulated SOA. The MCM v3.1 aerosol module was used as a reference benchmark for the production of an optimized SOA module suitable for use with the CRI v2 and its derivatives.[12] The resultant aerosol module includes an emission of primary organic aerosol (POA) and 14 SOA species representing the gas phase absorption of low volatility products. There are three species representing aromatic hydrocarbons, ten terpene-derived species and one isoprene-derived species. The large set of terpene derived species is needed as terpene derivatives were found to be important SOA precursors over the full range of pollution conditions. In contrast, SOA derived from aromatic hydrocarbons and isoprene are found to only be significant at high and low pollution levels, respectively, allowing a more limited number of surrogates to be used.[12]

References.

1. Archibald, A.T. et al. Impacts of mechanistic changes on HO_x formation and recycling in the oxidation of isoprene. *Atmos. Chem. Phys.* 10, 1-23 (2010).
2. Archibald, A.T. et al., Impacts of Formaldehyde Photolysis Rates on Tropospheric Chemistry. *Atmos. Sci. Letts*. 11, 33-38 (2010).
3. Cooke, M.C. et al. On the effect of a global adoption of various fractions of biodiesel on key species in the troposphere. *Int. J. Oil, Gas and Coal Tech*. 3, 88-103 (2010).
4. Henne, S. et al. Future emissions and atmospheric fate of HFC-1234yf from mobile air conditioners in Europe. *Env. Sci. Tech.* 46, 1650-1658 (2012).
5. Bacak, A. et al. Kinetics of the $HO_2 + NO_2$ Reaction: On the impact of new gas-phase kinetic data for the formation of HO_2NO_2 on HO_x, NO_x and HO_2NO_2 levels in the troposphere. *Atmos. Environ.* 45, 6414-6422 (2011).
6. Utembe, S.R. et al. Using a reduced Common Representative Intermediates (CRIv2-R5) Mechanism to Simulate Tropospheric Ozone in a 3-D Lagrangian Chemistry Transport Model. *Atmos. Environ.,* 44, 1609-1622 (2010).
7. Utembe, S.R. et al. Simulating Secondary Organic Aerosol in a 3-D Lagrangian Chemistry Transport Model using the reduced Common Representative Intermediates Mechanism (CRIv2-R5). *Atmos. Environ.* 45, 1604-1614 (2011).
8. Collins, W. et al. (1997) Tropospheric Ozone in a Global-Scale Three-Dimensional Lagrangian Model and Its Response to NO_X Emission Controls. *J. Atmos. Chem.* 26, 223-274 (1997).
9. Derwent, R. G. et al. Radiative forcing from surface NOx emissions: spatial and seasonal variations. *Climatic Change,* 88, 385-401(2008).
10. Watson, L.A. et al. A Common Representative Intermediates (CRI) mechanism for VOC degradation. Part 2: Gas phase mechanism reduction. *Atmos. Environ.* 42, 7196-7204 (2008).
11. Jenkin, M.E. et al. A Common Representative Intermediates (CRI) mechanism for VOC degradation. Part 1: Gas phase mechanism development. *Atmos. Environ.* 42, 7185-7195 (2008).
12. Utembe, S.R. et al. A Common Representative Intermediates (CRI) mechanism for VOC degradation. Part 3: Development of a secondary organic aerosol module. *Atmos. Environ*. 43, 1982-1990 (2009).
13. Johns, T.C. et al. The second Hadley Centre coupled ocean-atmosphere GCM:model description, spinup and validation. *Clim. Dynam.* 13, 103–134 (1997).
14. Stevenson, D.S. et al. Evolution of tropospheric ozone radiative forcing. *Geophys. Res. Letts.* 25, 3819–3822 (1998).
15. Simmons, A. J. & Burridge, D. M. An energy and angular-momentum conserving vertical finite-difference scheme and hybrid vertical coordinates. *Mon. Weather Rev.* 109,758–766 (1981).
16. Cullen, M.J. The unified forecast/climate model. *Meteorol. Mag*. 122, 81–94 (1993).
17. Collins, W. J. et al. The European regional ozone distribution and its links with the global scale for the years 1992 and 2015. *Atmos. Environ.* 34, 255–267 (1997).

18. Saunders, S. M. et al. Protocol for the development of the Master Chemical Mechanism, MCM v3 (Part A): tropospheric degradation of non-aromatic volatile organic compounds. *Atmos. Chem. Phys.* 3, 161–180 (2003).
19. Jenkin, M. E. et al. Development of a reduced speciated VOC degradation mechanism for use in ozone models. *Atmos. Environ.* 36, 4725–4734 (2002).
20. DeMore, W. B. et al. Chemical Kinetics and Photochemical Data for Use in stratospheric Modeling, Evaluation Number 10. JPL Publication 92-20, Jet Propulsion Laboratory, California Institute of Technology, Pasadena, CA (1992).
21. Sander, S. P. et al. Chemical Kinetics and Photochemical Data for Use in Atmospheric Studies: Evaluation Number 15. Technical report, NASA JPL Publications 06-2 (2006).
22. Atkinson, R. et al. Evaluated kinetic and photochemical data for atmospheric chemistry: Volume II - reactions of organic species. *Atmos. Chem. Phys.* 6, 3625–4055 (2006).
23. Hough. A., The calculation of photolysis rates for use in global tropospheric modelling studies. AERE Report R-13259 (1988).
24. Olivier, J. *et al.* Description of EDGAR Version 2.0: A set of global emission inventories of greenhouse gases and ozone-depleting substances for all anthropogenic and most natural sources on a per country basis and on 1 degree x 1 degree grid. (Netherlands Environmental Assessment Agency, 1996).
25. Cofala, J. et al. Scenarios of global anthropogenic emissions of air pollutants and methane up to 2030. Technical report, International Institute for Applied systems Analysis, Laxenburg, Austria (2005).
26. Granier, C. et al. POET, a database of surface emissions of ozone precursors, http://www.aero.jussieu.fr/projet/ACCENT/POET.php, (2005).
27. Mikaloff-Fletcher et al. CH4 sources estimated from atmospheric observations of CH4 and its 13C/12C isotopic ratios: 1. Inverse modeling of source processes. *Global Biogeochem. Cy.* 18, doi: 10.1029/2004GB002223 (2004).
28. Houweling, S. et al. The modeling of tropospheric methane- How well can point measurements be reproduced by a global model? *J. Geophys. Res.* 105, 8981–9002 (2000).
29. Henze, D. et al. Global modeling of secondary organic aerosol formation from aromatic hydrocarbons: high-vs. low-yield pathways. *Atmos. Chem. Phys.* 8, 2405-2420 (2008).
30. Andreae, M. & Merlet, P. Emission of trace gases and aerosols from biomass burning, *Global Biogeochemical Cycles* 15, 955-966 (2001).
31. Dentener, F. et al. Emissions of primary aerosol and precursor gases in the years 2000 and 1750 prescribed data-sets for AeroCom. *Atmos. Chem. Phys.* 6, 4321–4344 (2006).
32. Randerson, J. T. et al. Global fireemissions database, version 2 (gfedv2.1). data set. available on-line [http://daac.ornl.gov/].Technical report, Oak Ridge National Laboratory Distributed Active Archive Center, Oak Ridge, TN (2007).
33. Seinfeld J. H. & Pandis S. N. Atmospheric Chemistry and Physics. Wiley, 2006.
34. Li, D. & Shine. K. P. A 4-dimensional ozone climatology for UGAMP models, Internal Rep.35, Technical report, University of Reading (1995).

35. Murphy, D. M. & Fahey, D. W. An estimate of the flux of stratospheric reactive nitrogen and ozone into the troposphere. *J. Geophys. Res.* 99, 5325–5332 (1994).
36. Price, C. & Rind, D. A simple lightning parameterization for calculating global lightning distributions. J. Geophys. Res. 97, 9919–9933 (1992).
37. Penner, J.E. *et al* IPCC Special Report on Aviation and the Global Atmosphere. Technical report, tech. rep., the Intergovernmental Panel on Climate Change, 1999.
38. Jenkin, M.E. Modelling the formation and composition of secondary organic aerosol from α- and β-pinene ozonolysis using MCMv3. *Atmos. Chem. Phys.* 4, 1741–1757 (2004).
39. Johnson, D. et al. Simulating the Formation of Secondary Organic Aerosol from the Photooxidation of Toluene. *Environ. Chem.* 1, 150–165 (2004).
40. Johnson, D., Utembe, S. R. & Jenkin, M. E. Simulating the detailed chemical composition of secondary organic aerosol formed on a regional scale during the TORCH 2003 campaign in the southern UK. *Atmos. Chem. Phys.* 6, 419–431 (2006).
41. Johnson, D. et al. Simulating regional scale secondary organic aerosol formation during the TORCH 2003 campaign in the southern UK. *Atmos. Chem. Phys.* 6, 403–418 (2006).
42. Utembe, S. R. et al. Modelling the ambient distribution of organic compounds during the August 2003 ozone episode in the southern UK Modelling the ambient distribution of organic compounds during the August 2003 ozone episode in the southern UK. *Faraday Discuss.* 130, 311–326 (2005).
43. Pankow, J. F. Absorption model of gas/particle partitioning of organic compounds in the atmosphere. *Atmos. Environ.* 28,185–188 (1994).
44. Stein, S. E. & Brown, R. L. Estimation of normal boiling points from group contributions. *J. Chem. Inf. Comp. Sci.* 34, 581–587 (1994).
45. Baum, E. J. Chemical Property Estimation: Theory and Application. CRC Press, Boca Raton, FL (1998).